



# Microstructure Evolution and Mechanical Properties of Ultra-Fine Grain AlCrFe<sub>2</sub>Ni<sub>2</sub>W<sub>x</sub> High-Entropy Alloys

Shougang Duan<sup>1</sup> · Yufeng Yang<sup>1</sup> · Yong Dong<sup>1</sup> · Yu Wang<sup>2</sup> · Beibei Jiang<sup>3</sup> · Chuanqiang Li<sup>1</sup> · Zhengrong Zhang<sup>1</sup>

Received: 9 August 2022 / Accepted: 12 October 2022 / Published online: 14 November 2022  
© The Author(s) under exclusive licence to The Korean Institute of Metals and Materials 2022

## Abstract

Ultra-fine grain AlCrFe<sub>2</sub>Ni<sub>2</sub>W<sub>x</sub> ( $x = 0.1, 0.2, 0.3, 0.4$ ) alloys were designed and prepared by vacuum arc melting, and corresponding microstructural evolution and mechanical properties were investigated. All of the alloys show a mixed structure with FCC + BCC (B2) + TCP phases. The addition of W element has a significant effect on the formation mechanism of the morphology, which promotes the transition from FCC phase to  $\mu$  phase and inhibits the spinodal decomposition of BCC phase. With the increase of W content, more  $\mu$  phase precipitates from the FCC phase and grain boundaries. After the dissolution of W element into matrix, the formed oversaturated solid solution and precipitated  $\mu$  phase have the effect of solid solution strengthening and second phase strengthening, respectively. The yield strength and Vickers hardness increases from 765 to 1319.6 MPa and HV 332.2 to HV 461.8, respectively. The addition of W element enhances the strength of the alloys but reduced ductility. The AlCrFe<sub>2</sub>Ni<sub>2</sub>W<sub>0.1</sub> alloy exhibits outstanding comprehensive mechanical properties, with its fracture strength reaching 2726.5 MPa and a considerable compressive strain of 43.3%, which implies promising potential engineering application.

**Keywords** High-entropy alloy · Microstructural evolution · Mechanical properties · Strengthening · Formation mechanism

## 1 Introduction

In recent decades, high-entropy alloys (HEAs) or multi-component alloys (MCAs) are considered to be one of the three major breakthroughs in alloying theory, which break the traditional design concept of using one or two elements as the main elements and adjusting properties by adding some other trace elements [1]. The HEAs or MCAs were proposed by Yeh et al. and Cantor et al. in 2004 and generally include at least five principal elements with equal or near-equal atomic ratios, and each ranging from 5 to 35% [2, 3]. Compared to conventional alloys, HEAs have four

major effects [2]: (1) thermodynamics: high-entropy effect, (2) structures: severe lattice-distortion effect, (3) kinetics: sluggish diffusion effect, and (4) properties: cocktail effects. These effects make the high-entropy alloys possess the outstanding properties, such as excellent strength-ductility synergy, high and low-temperature strength, good corrosion resistance, etc. [4–11]. Thus, HEAs have a wide range of applications in the fields of machinery, electronics, chemicals, aerospace, and military industry [12–14].

Normally, due to the high entropy effect, the solid solution in HEAs tends to form a simple face-centered cubic (FCC) or body-centered cubic (BCC) structure, and the hexagonal close-packed (HCP) structure only exists in a few HEAs, instead of other intermetallic phases or complex phases [2, 3]. The properties of HEAs mainly depend on the type of solid solution formed. The single phase with FCC-structured HEAs generally have good ductility and poor strength, while the BCC-structured HEAs have higher strength but poor ductility [15–17]. In recent years, scholars have mainly focused on dual-phase HEAs, which are expected to exhibit balanced mechanical properties, e.g., both high strength and good ductility [18–26]. The eutectic high entropy alloys (EHEAs), firstly proposed by Lu et al.,

✉ Yong Dong  
dongyong5205@163.com

✉ Yu Wang  
wangyu@nuc.edu.cn

<sup>1</sup> School of Materials and Energy, Guangdong University of Technology, Guangzhou 510006, China

<sup>2</sup> School of Materials Science and Engineering, North University of China, Taiyuan 030051, China

<sup>3</sup> GDUT Analysis and Test Center, Guangdong University of Technology, Guangzhou 510006, China

which perfectly combines the characteristics of the eutectic alloy and EHEAs, has attracted widespread attention [18]. The AlCoCrFeNi<sub>2.1</sub> EHEA not only achieves a balance between strength and ductility but also has good castability. Subsequently, increasing attention is given to the alloy system A–(Co)–Cr–Fe–Ni [27–33]. To reduce the cost without affecting mechanical properties, Dong et al. designed a novel Co-free dual-phase AlCrFe<sub>2</sub>Ni<sub>2</sub> alloy, which is composed of a “noodle-like” FCC phase intertwined with a spinodal decomposed BCC phase of an almost equal volume fraction [28]. The “noodle-like” structure also named as an ultra-fine vermicular microstructure (UVM) [29]. The as-cast AlCrFe<sub>2</sub>Ni<sub>2</sub> alloy exhibits outstanding mechanical properties, with a tensile yield strength of 796 Mpa, a breaking strength of 1266.5 Mpa, and an elongation of 15.7% [28].

In addition, alloying is one of the most effective ways to improve the mechanical properties of HEAs [34–36]. The formation of TCP phase could be effectively promoted by adding transition elements into the HEAs [37, 38]. Typical brittle phase often results in severe embrittlement of alloys, but a small amount of the second phase could lead to a reinforcing effect. Recently, the microstructure evolution and mechanical properties of AlCrFe<sub>2</sub>Ni<sub>2</sub>(MoNb)<sub>x</sub> alloys were reported by Li et al. [34]. With the addition of Mo and Nb content, a novel Laves phase was formed and the microstructural morphology changes significantly. The yield strength of the alloy was significantly improved by the second phase strengthening. Niu et al. investigated a series of alloys CoCrFeNiW<sub>x</sub> (in molar ratio, x=0, 0.2, 0.5). All alloys x < 0.2 displayed single FCC phase. For CoCrFeNiW<sub>0.5</sub> alloy, besides the FCC phase, an μ-W<sub>6</sub>Fe<sub>7</sub> type μ phase with TCP structure precipitates from the matrix. The addition of W significantly reduces the grain size, and enhance the Vickers hardness and yield strength of W-free alloy [37].

However, the effect of W elements on HEAs with spinodal decomposition structures has not been reported. In this study, the AlCrFe<sub>2</sub>Ni<sub>2</sub> was selected as the matrix alloy and W elements was used as adding element. We designed and prepared AlCrFe<sub>2</sub>Ni<sub>2</sub>W<sub>x</sub> (in molar ratio, x=0.1, x=0.2, x=0.3 x=0.4) series alloy. The effect of W element on the microstructural evolution and mechanical properties of AlCrFe<sub>2</sub>Ni<sub>2</sub>W<sub>x</sub> alloys were systematically investigated.

## 2 Chemical Composition Design and Experimental Methods

### 2.1 Chemical Composition Design

For the formation and stability of HEAs, Yeh et al. suggested that high mixing entropy ( $\Delta S_{\text{mix}}$ ) is the main factor that promotes the formation of multi-principal component solid solution [2]. However, with further study of HEAs, it

is recognized that the  $\Delta S_{\text{mix}}$  effect alone is not enough to completely control the formation of solid solution. Other factors, such as the valence electron concentration (VEC), the enthalpy of mixing ( $\Delta H_{\text{mix}}$ ), the electronegativity differences ( $\Delta X$ ), and the atomic radius differences ( $\delta$ ), can also influence the formation and stability of solid solutions in HEAs. Zhang et al. proposed the application of  $\Delta S_{\text{mix}}$ ,  $\Delta H_{\text{mix}}$ , and  $\delta$  to determine the formation of solid solution in high entropy alloys [39]. It was determined that solid solution is formed stably when  $\delta \leq 6.5\%$ ,  $-15 \leq \Delta H_{\text{mix}} \leq 5$  kJ/mol, and  $12 \leq \Delta S_{\text{mix}} \leq 17.5$  J/K mol. Guo et al. [40] investigated the effect of VEC on the stability of FCC and BCC solid solutions in HEAs, and the results are as follows: The FCC phase is more stable when  $\text{VEC} \geq 8.6$ ; the BCC phase will be formed when  $\text{VEC} < 6.87$ , and the HEAs tends to form FCC + BCC dual-phases when  $6.87 \leq \text{VEC} < 8.6$ . A new physical parameter, i.e., the electronegativity differences ( $\Delta X$ ) proposed by Dong et al., can also effectively predict the formation of TCP phases [41]. It was found that the TCP phase could be formed when  $\Delta X > 0.133$ . The calculation formulas of  $\Delta S_{\text{mix}}$ ,  $\Delta H_{\text{mix}}$ ,  $\delta$ , VEC, and  $\Delta X$  can be obtained in the Refs [39–41]

Based on the above empirical parameters, we have designed AlCrFe<sub>2</sub>Ni<sub>2</sub>W<sub>0.1</sub>, AlCrFe<sub>2</sub>Ni<sub>2</sub>W<sub>0.2</sub>, AlCrFe<sub>2</sub>Ni<sub>2</sub>W<sub>0.3</sub> and AlCrFe<sub>2</sub>Ni<sub>2</sub>W<sub>0.4</sub> alloys, and the corresponding parameters were calculated, as shown in Table 1. According to the calculation results, we predict that FCC and BCC phases still exist in these four alloys, and a new TCP phase may be formed.

### 2.2 Experimental Methods

The button-like ingots of the AlCrFe<sub>2</sub>Ni<sub>2</sub>W<sub>x</sub> (x=0.1, 0.2, 0.3, 0.4, denoted as W01, W02, W03, W04, respectively) alloys were synthesized by vacuum arc furnace under a pure argon (Ar) atmosphere. All ingots were remelted at least five times with electromagnetic stirring to ensure the chemical homogeneous. The raw materials used in this study were pure Al, Cr, Fe, Ni, and W, all of which had a purity above 99.9 wt%. All experimental samples were taken from the master ingots by wire-electrode cutting. The phases and crystal structures of all samples were identified

**Table 1** The thermodynamic parameters  $\Delta H_{\text{mix}}$ ,  $\Delta S_{\text{mix}}$ ,  $\delta$ ,  $\Delta X$ , and VEC for the AlCrFe<sub>2</sub>Ni<sub>2</sub>W<sub>x</sub> alloys

| Alloys | $\Delta H$ (KJ/mol) | $\Delta S$ (J/K mol) | $\delta$ (%) | $\Delta X$ | VEC  |
|--------|---------------------|----------------------|--------------|------------|------|
| W0     | − 11.11             | 11.05                | 5.281        | 0.1164     | 7.5  |
| W01    | − 10.85             | 11.57                | 5.38         | 0.1361     | 7.48 |
| W02    | − 10.59             | 11.88                | 5.47         | 0.1523     | 7.45 |
| W03    | − 10.35             | 12.12                | 5.55         | 0.1660     | 7.43 |
| W04    | − 10.12             | 12.31                | 5.62         | 0.1778     | 7.41 |

with an X-ray diffraction (XRD, EMPYREAN with Cu radiation target) at a speed of  $4^\circ \text{ min}^{-1}$  in the  $2\theta$  scanning ranging from  $20^\circ$  to  $100^\circ$ . For microstructural observation, the testing samples were ground, polished, and etched with alcohol dilute aqua regia (etching solution: 3 ml HCl + 1 ml  $\text{HNO}_3$  + 8 ml  $\text{C}_2\text{H}_5\text{OH}$ ). The microstructures of the etched samples were characterized by field-emission scanning electron microscopy (SEM, Zeiss supra-55) with energy dispersive spectroscopy (EDS). Thin-film samples of W02 and W03 alloys were prepared by mechanical grinding to  $\sim 70$  nm thickness followed by twin-jet electropolishing (electrolyte: 90% ethanol + 10% perchloric acid, in vol%), and then characterized by transmission electron microscopy (TEM, Talos F200S) with energy dispersive spectrometry (EDS). The microhardness of  $\text{AlCrFe}_2\text{Ni}_2\text{W}_x$  alloys were measured using a Vickers hardness tester (MH-5L) with a load of 1000 g and a duration of 15 s. To reduce experimental error, each sample were tested at least seven times. The maximum and minimum data were removed to obtain the average experimental data. The cylindrical samples with a diameter of 5 mm and a length of 10 mm were prepared from the master ingots for quasi-static compression testing at room temperature with a strain rate of  $1 \times 10^{-3} \text{ s}^{-1}$ . Three compression tests were required for each set of samples to ensure the repeatability of the test. The compression fracture morphologies of the  $\text{AlCrFe}_2\text{Ni}_2\text{W}_x$  alloys were examined by scanning electron microscopy (SEM, Zeiss supra-55).

### 3 Results and Discussion

#### 3.1 Crystal Structures Analysis

The X-ray diffraction (XRD) patterns of the as-cast  $\text{AlCrFe}_2\text{Ni}_2\text{W}_x$  ( $x = 0, 0.1, 0.2, 0.3, 0.4$ ) alloys are shown in Fig. 1. It can be seen that the  $\text{AlCrFe}_2\text{Ni}_2$  (marked as W0) alloy exhibits a mixture of FCC phase, disordered BCC phase, and ordered BCC (B2) phase. The presence of ordered BCC (B2) phase can be proved by the (100) super-lattice peak. Noted, the modulated microstructure often shows overlapping disordered BCC and B2 Bragg reflections due to their same crystal structure and similar lattice parameters. This phenomenon is also found in other HEAs [19]. A new weak diffraction peak of  $\mu$  phase can be observed from the XRD pattern when the content of W is 0.1. With the content of W further increases, the content of  $\mu$  phase increased and the intensity of diffraction peak of becomes higher, which indicates that the addition of W can promote the formation of  $\mu$  phase. The  $\mu$  phase is identified as a close-packed hexagonal lattice structure ( $a = b = 1.085 \text{ nm}$ ,  $c = 1.926 \text{ nm}$ ,  $\alpha = \beta = 90^\circ$ ,  $\gamma = 120^\circ$ ). Similar phase identification also has been reported in other literatures [37, 38]. The subsequent TEM results

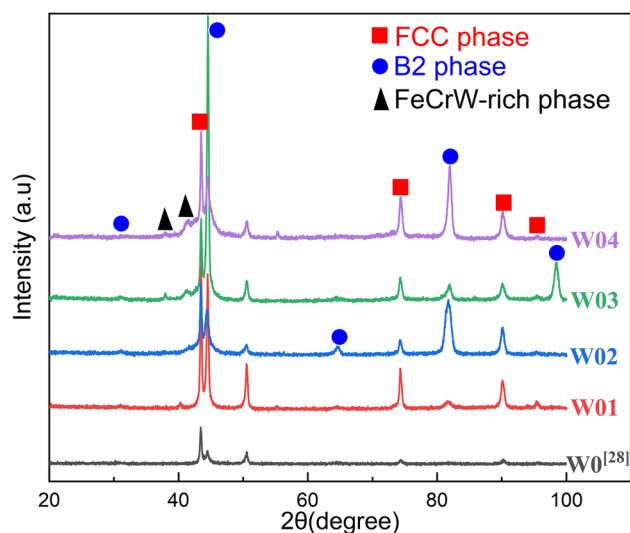


Fig. 1 XRD patterns of the  $\text{AlCrFe}_2\text{Ni}_2\text{W}_x$  alloys

Table 2 Lattice parameter variation of different phases in the  $\text{AlCrFe}_2\text{Ni}_2\text{W}_x$  alloys

| Alloys  | Lattice parameters (Å) |        |
|---------|------------------------|--------|
|         | FCC                    | BCC    |
| W0 [29] | 3.554                  | 2.889  |
| W01     | 3.6044                 | 2.8774 |
| W02     | 3.6051                 | 2.8826 |
| W03     | 3.6013                 | 2.8748 |
| W04     | 3.6012                 | 2.8773 |

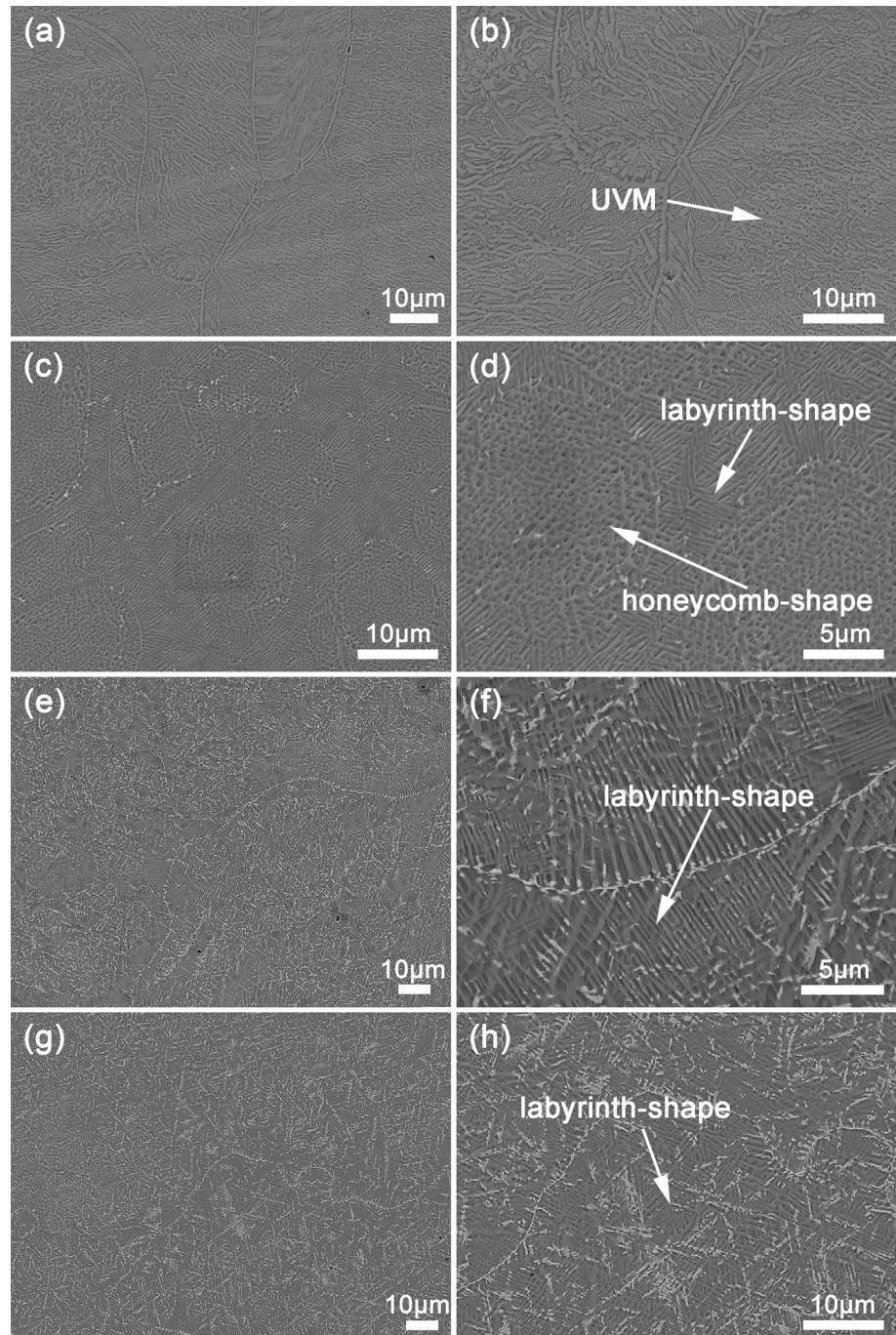
also confirmed the XRD results. The lattice parameters of the FCC phases and the BCC or B2 phases are calculated from the strongest peak  $(111)_{\text{FCC}}$  and peak  $(110)_{\text{BCC}}$  using the Bragg equation. The calculation results are shown in Table 2. It is worth noting that when  $x$  is 0.1, the lattice constant of FCC increases from 3.554 to 3.6044 Å, which may be due to the severe lattice distortion caused by the larger atomic radius of W element. When the content of W reaches 0.2, the lattice constant of FCC phase almost unchanged, which could be that the solid solubility of W element in the FCC phase has reached the limit. With further increase of W content, the lattice constant of FCC decreases, which could be due to the formation of  $\mu$  phase, thereby leading to atomic reconstruct and release of the lattice stress. The atomic radius of Al, Cr, Fe, Ni, and W are 143 pm, 128 pm, 126 pm, 124 pm, and 139 pm, respectively. According to previous research, more Al elements could be identified in B2 phase [31]. Therefore, when the W atoms with a smaller atomic radius than Al dissolve into the B2 phase, the resulting lattice distortion is small and the lattice constant changes little, which is consistent with our calculation results.

For the prediction of solid solution phases in  $\text{AlCrFe}_2\text{Ni}_2\text{W}_x$  ( $x = 0.1, x = 0.2, x = 0.3, x = 0.4$ ) alloys, the predictions are in good agreement with the experimental results. These parameters are highly instructive for the design of HEAs, and they should be considered comprehensively during the material design process.

### 3.2 Microstructural Characterization

The SEM images of the as-cast  $\text{AlCrFe}_2\text{Ni}_2\text{W}_x$  ( $x = 0.1, 0.2, 0.3, 0.4$ ) alloys are shown in Fig. 2. In the previous study, Dong et al. designed a Co-free  $\text{AlCrFe}_2\text{Ni}_2$  (marked as W0) alloy whose microstructure consists of a large amount of disordered noodle-like phases and spinodal decomposition structures. After further TEM analysis, the noodle-like phase has an FCC structure, while the spinodal structure exhibits the BCC + B2 structures [28]. It can be seen from Fig. 2a,

**Fig. 2** SEM images of the  $\text{AlCrFe}_2\text{Ni}_2\text{W}_x$  alloys ( $x = 0.1, 0.2, 0.3, 0.4$ ): **a, c, e, and g** are the low magnification of W01, W02, W03, and W04 alloys, respectively; **b, d, f, and h** are the high magnification of W01, W02, W03, and W04 alloys, respectively



b that two distinct phases could be found in the W01 alloy, i.e., a disordered noodle-like phase (also named ultra-fine vermicular microstructure (UVM)) and an interconnected microstructure. According to previous literature reports [27, 28], the interconnected microstructure is a typical characteristic of nano-scale spinodal decomposition. This indicates that the microstructure of the alloy barely changes after adding trace of W element. As the W content increases, the microstructure of W02 alloy changes significantly, as shown in Fig. 2c, d. The W02 alloy shows the honeycomb-shape and labyrinth-shape structures, while the white precipitated phases are observed on the surface. These unique microstructures are highly similar to the sunflower-like eutectic colony structure in the  $\text{Al}_{0.75}\text{CrFeNi}$  alloy reported by Jiao et al. [30]. The labyrinth-shape structure is approximately 100 nm wide. Interestingly, the honeycomb-shape structures and labyrinth-shape structures are closely connected to each other, which implies they could have the same crystal structure. When the content of W further increases, the morphology of W03 and W04 alloys again evolves, as shown in Fig. 2e–h. It can be seen that W03 and W04 alloys are composed of labyrinth-shape structures and bright white precipitates. The white precipitates are enriched at grain boundaries. The chemical compositions of different regions in the as-cast  $\text{AlCrFe}_2\text{Ni}_2\text{W}_x$  alloys by SEM–EDS are shown in Table 3. From the SEM–EDS results, the UVM phase contains more Fe, Cr and Ni elements, while the spinodal structure contains more Al and Ni elements in W01 alloy. The light gray phase of W02, W03, and W04 alloys is rich in Fe and Cr elements, and the dark gray phase is rich in Al and Ni elements. The white precipitates in all alloys are rich in Fe, Cr, and W elements. Generally, for alloy system Al–Cr–Fe–Ni, the Al, Ni-rich in B2 phase, and the Fe,

Cr-rich in FCC phase [31]. Combined with the XRD and SEM–EDS results, it can be concluded that the UVM and light gray phase has FCC structure, the dark gray phase has the BCC/B2 phase, and the white precipitates is a FeCrW-Type  $\mu$  phase.

Even the addition amount of W element is small, it would not only have a significant effect on the phase composition of the  $\text{AlCrFe}_2\text{Ni}_2\text{W}_x$  alloys, but also on the anisotropy of the morphology. The phase volume fraction changes of the  $\text{AlCrFe}_2\text{Ni}_2\text{W}_x$  alloys are shown in Fig. 3. It seems counterintuitive that the volume fraction of BCC (B2) phase in W01 alloy is decrease from 48% to 45.8%, because W is BCC (B2) stabilizing element [42]. This result indicates that the stabilization effect of W on the BCC phase is weaker

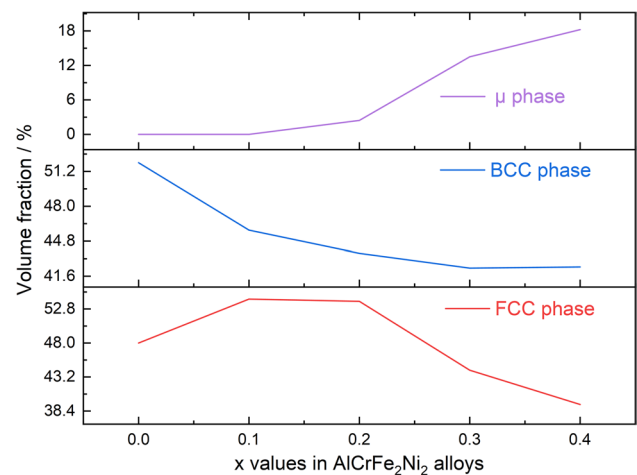


**Fig. 3** The volume fraction of different phases in  $\text{AlCrFe}_2\text{Ni}_2\text{W}_x$  alloys

**Table 3** SEM–EDS results of the different regions in the  $\text{AlCrFe}_2\text{Ni}_2\text{W}_x$  ( $x=0.1, 0.2, 0.3, 0.4$ ) alloys (at%)

| Alloy | Regions           | Chemical compositions (at%) |       |       |       |       |
|-------|-------------------|-----------------------------|-------|-------|-------|-------|
|       |                   | Al                          | Cr    | Fe    | Ni    | W     |
| W01   | Actual            | 17.70                       | 16.52 | 31.66 | 32.16 | 1.96  |
|       | Light gray phase  | 12.34                       | 17.49 | 35.97 | 32.21 | 1.99  |
|       | Dark gray phase   | 20.26                       | 17.02 | 29.64 | 30.88 | 2.20  |
| W02   | Actual            | 16.81                       | 16.09 | 31.47 | 31.93 | 3.70  |
|       | Light gray phase  | 14.87                       | 17.32 | 33.33 | 30.19 | 4.29  |
|       | Dark gray phase   | 18.63                       | 16.52 | 29.85 | 31.83 | 3.17  |
|       | White precipitate | 9.72                        | 21.81 | 33.83 | 20.41 | 14.23 |
| W03   | Actual            | 16.44                       | 15.95 | 31.11 | 31.94 | 4.56  |
|       | Light gray phase  | 6.51                        | 25.85 | 44.58 | 20.22 | 2.84  |
|       | Dark gray phase   | 21.43                       | 11.68 | 25.92 | 38.88 | 2.12  |
|       | White precipitate | 8.11                        | 19.37 | 31.79 | 19.14 | 21.59 |
| W04   | Actual            | 17.02                       | 15.53 | 30.62 | 31.77 | 5.05  |
|       | Light gray phase  | 11.86                       | 17.45 | 36.81 | 28.51 | 5.37  |
|       | Dark gray phase   | 18.36                       | 14.44 | 31.74 | 32.84 | 2.62  |
|       | White precipitate | 10.39                       | 18.52 | 30.45 | 18.27 | 22.37 |

than that of Al. This phenomenon was also reported in  $\text{CoCrFeNi}_2\text{Al}_{1-x}\text{W}_x$  alloys [42]. Moreover, according to Table 3, more W dissolves into the BCC phase in W01 alloys, which means that more Al elements are replaced, thereby weakening the stability of the BCC (B2) phase. However, when the addition of W element exceeds its solubility in FCC and B2 phases, the phase volume fraction of BCC phase is almost unchanged. Due to the poor mutual solubility of W element and other elements, W element is easily repelled to the solid–liquid interface during the solidification. When the temperature is lowered to a suitable temperature, the W element solidifies as a  $(\text{FeCr})_7\text{W}_6$ -type  $\mu$  phase at the grain boundary. The FCC phase is rich in Fe and Cr elements, which suggests the  $\mu$  phase is easier to precipitate from the FCC matrix. This well explains the reduction in FCC phase volume fraction from 54.2 to 39.33%.

To further confirm the phase structure, the TEM tests were performed on W02 and W03 alloys. Figure 4 shows the TEM analysis of the W02 and W03 alloys, including the bright-field TEM images and selected area electron diffraction (SAED) patterns. The SAED patterns in Fig. 4a2 proves that the BCC phase in W02 alloy has a superlattice-structure, indicating that the precipitated-like particles in the honeycomb-shape structure has an ordered BCC-structured, and the labyrinth structures is alternating FCC phase and B2 phase. The bright white microstructures in SEM images have dense hexagonal lattice crystal structure. Similar to W02 alloy, the BCC phase in W03 alloy also has a superlattice-structure, as shown in Fig. 4b2. The W03 alloy is also composed of FCC phase, ordered BCC phase and  $\mu$  phase.

Interestingly, most of the  $\mu$  phases are formed in the FCC matrix, which is worth further discussion. Figure 5 shows the element distribution of the W02 and W03 alloys by TEM-EDS. It can be seen that the B2 phase has the highest Al and Ni elements and the least amount of Fe, Cr, and W elements, while the FCC phase enrich Fe and Cr elements and has the middle amount of Al, Ni, and W elements. Compared with FCC phase, the  $\mu$  phase contains more W elements. The chemical composition of all phases in W02 and W03 alloys were analyzed by more accurate TEM-EDS, as shown in Table 4. The results indicate that the solubility of W element in FCC solid solution is much higher than that of in B2 solid solution.

### 3.3 Phase Transformation Pathways

The composition, morphology, size and volume fraction of the constituent phases play an important role in the mechanical properties of the HEAs. Combined with the above XRD, SEM and TEM analysis, the addition of different W content has a significant effect on the morphology and crystal structure of  $\text{AlCrFe}_2\text{Ni}_2$  alloy, which means that the solidification behavior has changed. For the  $\text{AlCrFe}_2\text{Ni}_2$  alloy with distinctive microstructures, Ulrike Hecht et al. investigated its phase transformation pathways [29]. With the cooling rate increases from low to high, three types of conventional Widmanstätten microstructure (CWM), ultrafine vermicular microstructure (UVM), and ultrafine micro-platelet microstructure could be formed, respectively. The relevant transformation pathways are shown in Fig. 6. Moreover,

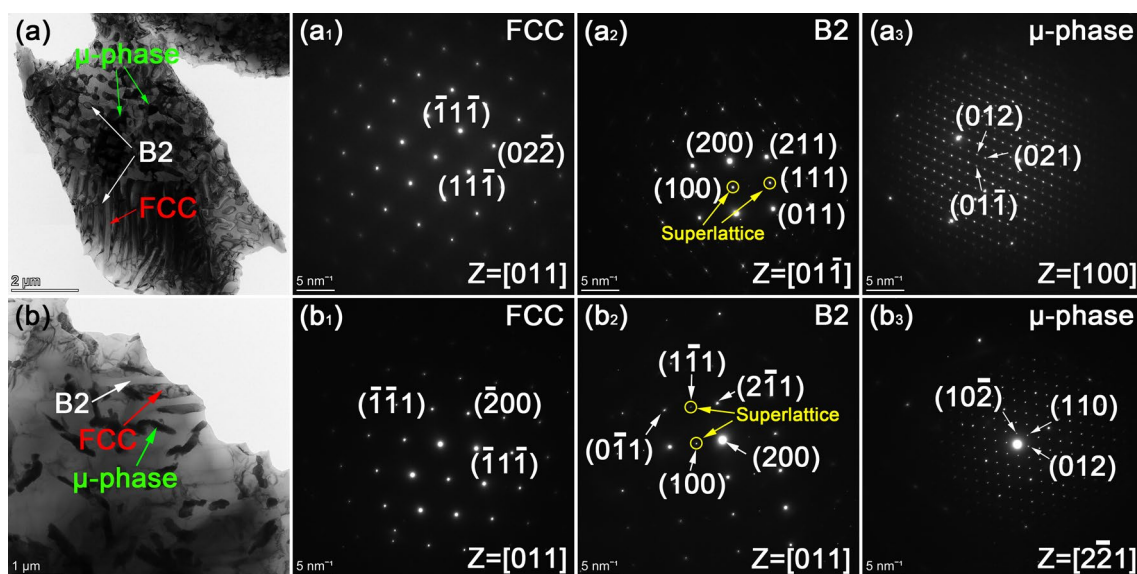


**Fig. 4** TEM analysis of the W02 and W03 alloys. **a** Bright-field image of the honeycomb-shape, labyrinth microstructures and precipitates in as-cast W02 alloy; **a<sub>1</sub>–a<sub>3</sub>** SAED patterns in as-cast W02

alloy; **b** Bright-field image of the braided structures and precipitates in as-cast W03 alloy; **b<sub>1</sub>–b<sub>3</sub>** SAED patterns in as-cast W03 alloy

**Fig. 5** TEM-EDS maps of the W02 and W03 alloys: **a** W02 alloy; **b** W03 alloy

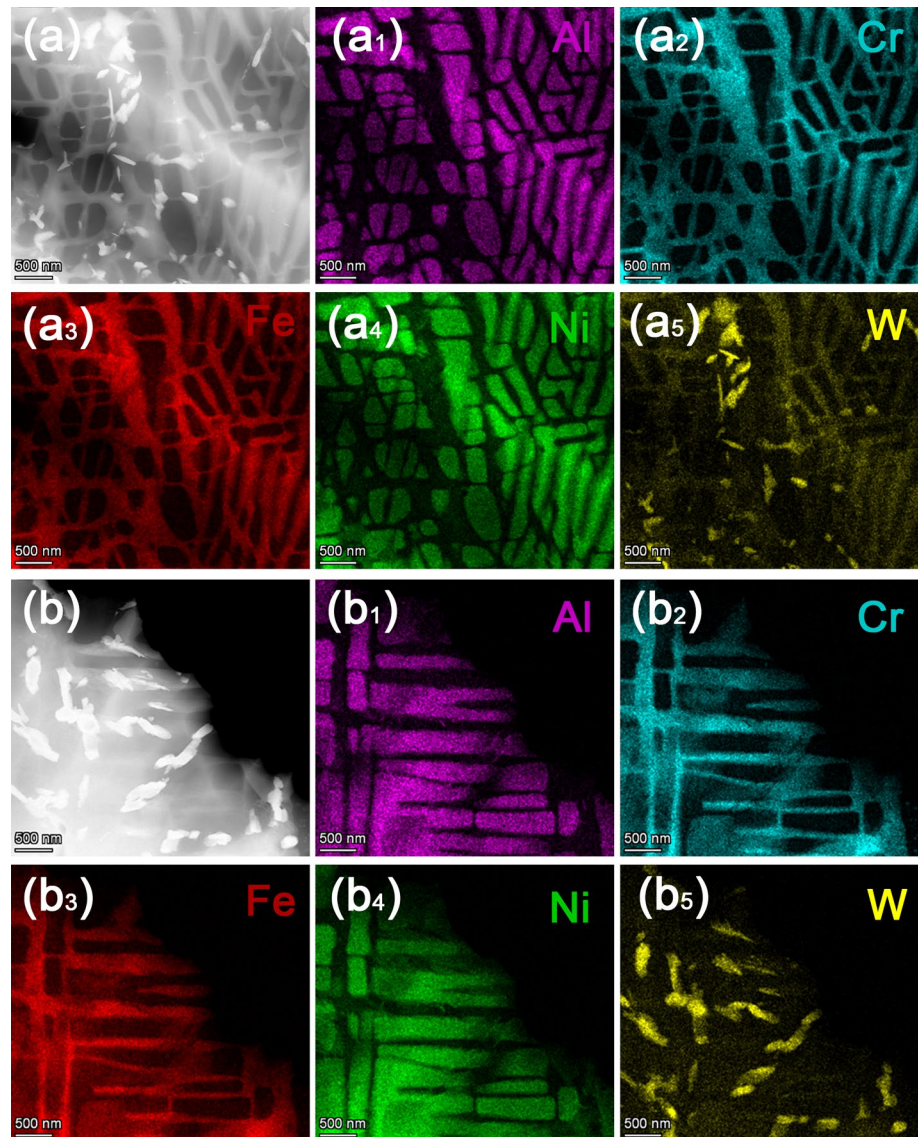


**Table 4** Chemical composition of FCC, B2, and  $\mu$  phases in as-cast W02 and W03 alloys by TEM-EDS (at%)

| Alloys        | Phases   | Al   | Cr   | Fe   | Ni   | W    |
|---------------|----------|------|------|------|------|------|
| W02 (TEM-EDS) | FCC      | 1.6  | 29.9 | 53.2 | 13.1 | 2.2  |
|               | B2       | 35.3 | 2.8  | 14.7 | 46.7 | 0.6  |
|               | FeW-rich | 1.0  | 29.3 | 40.7 | 9.7  | 19.3 |
| W03 (TEM-EDS) | FCC      | 5.9  | 19.7 | 46.8 | 23.2 | 4.4  |
|               | B2       | 32.0 | 4.2  | 15.0 | 47.9 | 1.0  |
|               | FeW-rich | 3.6  | 25.9 | 42.4 | 7.2  | 21.0 |

according to the Ulrike Hecht et al., the plate-like FCC phase requires a small undercooling for formation before the spinodal decomposition. From the Fig. 2a, b, only a small amount of plate-like morphology with short length can be observed in W01 alloy, and this phenomenon is explained as follows: during the solidification process, the W element is easily repelled to the front of the liquid surface due to

poor miscibility with other elements, which improves the undercooling of the W01 alloy and inhibits the nucleation and growth of the FCC phase with plate-like morphology. Therefore, the alloy of W01 mainly consists of UVM and spinodal structure.

In the W02 alloy, ultra-fine honeycomb-shape and labyrinth-shape structures can be observed, which are very rare

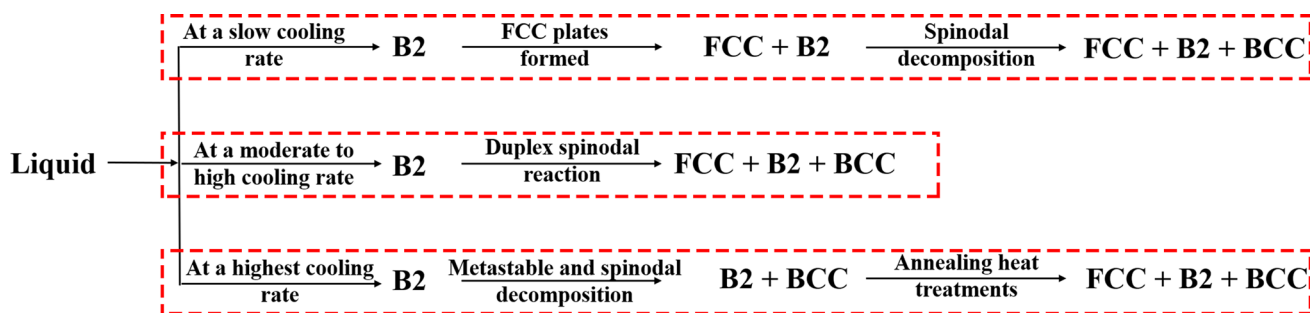


Fig. 6 Three transformation pathways of the AlCrFe<sub>2</sub>Ni<sub>2</sub> alloy

in HEAs. A similar morphology was also reported in the Al<sub>0.75</sub>CrFeNi alloy with BCC + B2 structure reported by Jiao et al., in which they called a sunflower-like eutectic morphology [30]. Based on their explanation of the formation mechanism of Al<sub>0.75</sub>CrFeNi alloy, we infer that a similar eutectic reaction occurs during the solidification of W02 alloy. Particularly, during the solidification process of W02 alloy, the parent phase is not B2 phase but FCC phase. The parent FCC is firstly formed in the W-rich regions. As the temperature decreases, the B2 phase particle precipitates from the parent FCC phase, and eutectic reaction occurs in the remaining liquid, consequently forming an ultra-fine labyrinth-shape eutectic morphology with FCC + B2 structure. Furthermore, due to the rapid cooling rate, W element will be precipitated in the oversaturate parent FCC solid solution forming FeCrW-type  $\mu$  phase, as shown in Fig. 2c, d. The corresponding transformation pathway are as follows: L (liquid)  $\rightarrow$  L + parent FCC  $\rightarrow$  FCC (parent and eutectic FCC phase) + B2 (precipitate and eutectic B2 phase)  $\rightarrow$  FCC + B2 +  $\mu$ . No honeycomb-shape structure could be observed in the W03 and W04 alloys, and only a finer labyrinth-shape structure, which implies that no parent phase is formed and only a eutectic reaction occurs. The transformation path along the labyrinth-shape structure are as follows: L  $\rightarrow$  FCC + B2  $\rightarrow$  FCC + B2 +  $\mu$ .

### 3.4 Mechanical Properties

Figure 7 shows the Vickers hardness of the as-cast AlCrFe<sub>2</sub>Ni<sub>2</sub>W<sub>x</sub> alloys. The detailed mechanical properties such as yield strength, ( $\sigma_s$ ), fracture strength, ( $\sigma_b$ ), fracture strain, ( $\epsilon$ ), and Vickers hardness are listed in Table 5. With the addition of W content, the Vickers hardness of the as-cast AlCrFe<sub>2</sub>Ni<sub>2</sub>W<sub>x</sub> alloys initially increases rapidly and then slowly. The rapid increase in hardness is attributed to two main factors: The first one is the large lattice distortion and significant solid solution strengthening caused by the dissolved W atoms with large radius in the FCC and BCC/B2 phases. The second one is the formation of the  $\mu$  phase and the increase of its volume fraction by W addition. The slow

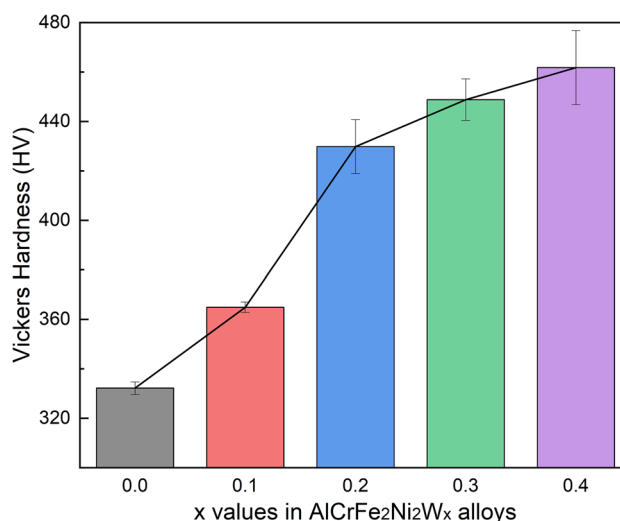


Fig. 7 The variations in Vickers hardness of the AlCrFe<sub>2</sub>Ni<sub>2</sub>W<sub>x</sub> alloys

Table 5 The mechanical properties of AlCrFe<sub>2</sub>Ni<sub>2</sub>W<sub>x</sub> alloys

| Alloys  | Yield strength (MPa) | Fracture strength (MPa) | Fracture strain (%) | Hardness (Hv) |
|---------|----------------------|-------------------------|---------------------|---------------|
| W0 [43] | 796.5                | –                       | –                   | 332.2 ± 2.5   |
| W01     | 973.7                | 2726.5                  | 43.3                | 364.9 ± 2.1   |
| W02     | 1181.7               | 2544.4                  | 32.1                | 429.8 ± 10.9  |
| W03     | 1219.5               | 2582.1                  | 26.3                | 448.8 ± 8.4   |
| W04     | 1319.6               | 2304.7                  | 27.6                | 461.8 ± 14.9  |

increase in hardness in stage II is due to the limited solubility of W atoms in the FCC and B2 phases and only the increase in the volume fraction of the  $\mu$  phase.

Figure 8 shows the quasi-static compressive engineering stress–strain curves of the as-cast AlCrFe<sub>2</sub>Ni<sub>2</sub>W<sub>x</sub> alloys at room temperature. The results indicate that the content of W has a significant influence on the compressive performance of the AlCrFe<sub>2</sub>Ni<sub>2</sub>W<sub>x</sub> alloys. The W0 alloy has good compression performance and no fracture occurs when the



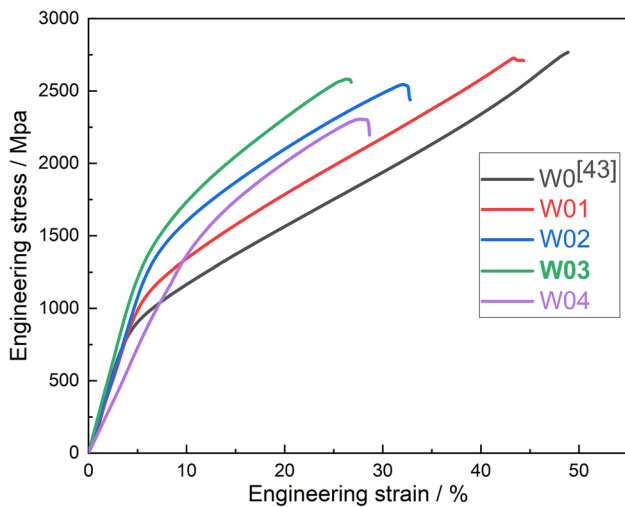


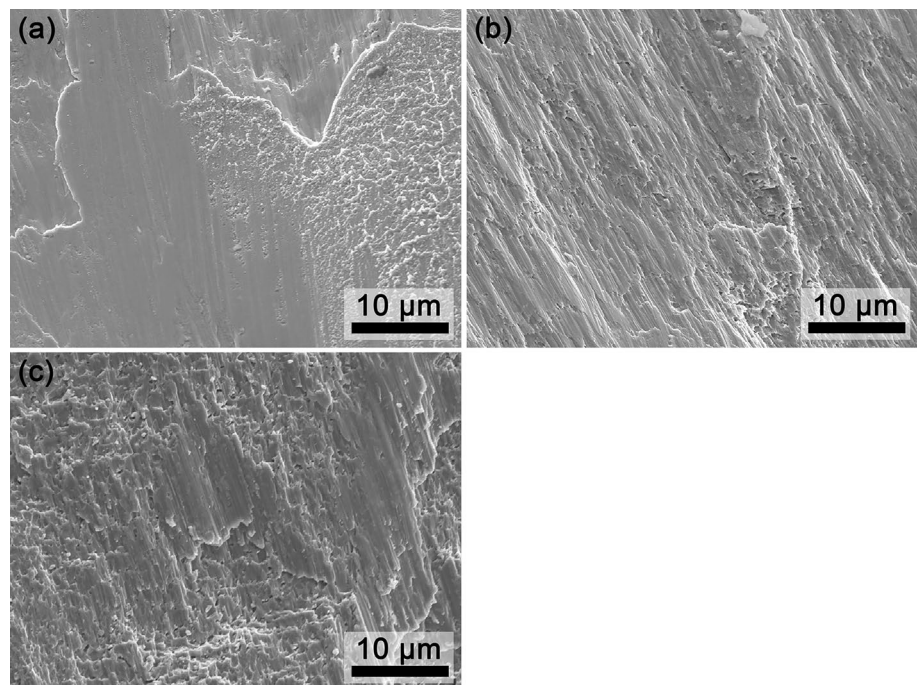
**Fig. 8** Compressive engineering stress–strain curves of the  $\text{AlCrFe}_2\text{Ni}_2\text{W}_x$  alloys

engineering compressive strain reaches 50% [43]. According to previous research, the phase interface between the BCC and B2 phases in the W0 alloy is completely coherent, and the Kurdjumov–Sachs orientation relationship between FCC phase and BCC phase is nearly perfect, which play an important role in improving the strength of W0 alloy [27]. In addition, the large volume fraction of the softer FCC phase provides better ductility, thus resulting in excellent mechanical properties of W0 alloy. With the addition of W, the yield strength ( $\sigma_s$ ) increases significantly from 796.5

to 1319.6 MPa, while the fracture strain ( $\sigma_b$ ) and plastic strain ( $\epsilon$ ) decrease to 2304.7 MPa and 26.3%, respectively. All alloys have good plasticity and work-hardening ability. The increase of yield strength ( $\sigma_s$ ) is mainly attributed to the following two factors: the first one is that W elements is partially dissolved in the FCC and BCC/B2 phases, the lattice distortion caused by larger atomic radius resulted in the solid solution strengthening effect. Furthermore, with the increase of W content, the  $\mu$  phase with TCP structure precipitates at FCC phase and grain boundary, and its volume fraction increases with the increase of W content. As a hard phase, the  $\mu$  phase distributes in the matrix and hinders the movement of dislocations during deformation process, which improves the yield strength. This way of strengthening is named as the second phase strengthening. The higher  $\mu$  phase content, the more significant effect of the second phase strengthening. However, due to the stress concentration caused by the massive entanglement of dislocations near the  $\mu$  phase, the cracks will preferentially initiate and fracture there. The plasticity of the alloy decreases significantly with increasing W content.

Figure 9 shows the compression fracture surface of the  $\text{AlCrFe}_2\text{Ni}_2\text{W}_x$  alloys (W01 and W01 alloy excluded). The samples of W01 alloys did not fracture when the compressive strains reach 50%, but a visible crack was observed on the lateral surface. This is a typical shear fracture after severe compression deformation. Similar results also have been found in other reports [42]. The fracture surface of W02 alloy is shown in Fig. 9a. It can be seen that the fracture surface of W02 alloy mainly consists of flat features,

**Fig. 9** Fracture morphologies of the  $\text{AlCrFe}_2\text{Ni}_2\text{W}_x$  alloys: **a** W02 alloy; **b** W03 alloy; **c** W04 alloy



the cleavage fracture and debonding features are not observed, which means the surface of the W02 alloy has a strong bonding force and compression fracture mode is a typical plastic fracture under compression. The fracture surface of W03 alloy shows torn edges and cleavage steps, which indicates that the fracture pattern is quasi-cleavage fracture, as shown in Fig. 9b. For the W04 alloy, the high-density cleavage steps are presented in Fig. 9c, which is featured by a typical cleavage fracture.

## 4 Conclusion

In this study, ultra-fine grain AlCrFe<sub>2</sub>Ni<sub>2</sub>W<sub>x</sub> (x = 0.1, 0.2, 0.3, 0.4) alloys were designed and produced by vacuum arc melting. The crystal structures, microstructure, compressive properties, and Vickers hardness were investigated, and the main conclusions are as follows:

1. The as-cast AlCrFe<sub>2</sub>Ni<sub>2</sub>W<sub>x</sub> (x = 0.1, 0.2, 0.3, 0.4) alloys are composed of FCC phase, BCC (B2) phase, and  $\mu$  phase. The W element has a significant effect on the formation mechanism of the AlCrFe<sub>2</sub>Ni<sub>2</sub>W<sub>x</sub> alloy. The  $\mu$  phase is mainly precipitated from the FCC phase, and its volume fraction increases with increasing of W content.
2. The mechanical properties of AlCrFe<sub>2</sub>Ni<sub>2</sub>W<sub>x</sub> alloys are closely related to the content of W element. With the content of W increases, the volume fraction of  $\mu$  phase increase, the yield strength and hardness of the alloys increases from 765 to 1319.6 MPa and HV 332.2 to HV 461.8, but the compressibility decreases to 26.3%. The improvement of strength and hardness can be attributed to the following two factors: the first one is the solid solution strengthening effect of the addition of W elements. The second is that the  $\mu$  phase hinders the movement of dislocations, resulting in the second phase strengthening effect. Due to the hard fragility of the  $\mu$  phase, cracks can be more easily during plastic deformation, resulting in reduced compressibility.

**Acknowledgements** This research was supported by the National Natural Science Foundation of China (Nos. 51801029), the Natural Science Foundation of Guangdong Province (No. 2022A1515012591), and the innovation and entrepreneurship training program for college students of Guangdong University of Technology (Nos. xj202111845622, xj202111845644).

## Declarations

**Conflict of interest** The authors declare that they have no known competing financial interests or personal relationships that could have appeared to influence the work reported in this paper.

## References

1. S. Ranganathan, *Curr. Sci. India* **85**, 1404 (2003)
2. J.W. Yeh, S.K. Chen, S.J. Lin, J.Y. Gan, T.S. Chin, T.T. Shun, C.H. Tsau, S.Y. Chang, *Adv. Eng. Mater.* **6**, 299 (2004)
3. B. Cantor, I.T.H. Chang, P. Knight, A.J.B. Vincent, *Mater. Sci. Eng. A* **375**, 213 (2004)
4. Y. Zhang, T.T. Zuo, Z. Tang, M.C. Gao, K.A. Dahmen, P.K. Liaw, Z.P. Lu, *Prog. Mater. Sci.* **61**, 1 (2014)
5. Y. Dong, S.G. Duan, X. Huang, C.Q. Li, Z.R. Zhang, *Mater. Lett.* **294**, 129778 (2021)
6. D.B. Miracle, O.N. Senkow, *Acta Mater.* **122**, 448 (2017)
7. P. Wang, Y.F. Wang, F. Cui, X.J. Yang, A.G. Pan, W.C. Wu, *J. Alloys Compd.* **918**, 165602 (2022)
8. C.Q. Shu, Z.J. Yao, X.L. Li, W.B. Du, X.W. Tao, H.M. Yang, *Phys. B* **638**, 413834 (2022)
9. T. Yang, Y.L. Zhao, Y. Tong, Z.B. Jiao, J. Wei, J.X. Cai, X.D. Han, D. Chen, A. Hu, J.J. Kai, K. Lu, Y. Liu, C.T. Liu, *Science* **362**, 933 (2018)
10. Y. Dong, Z.Q. Yao, X. Huan, F.M. Du, C.Q. Li, A.F. Chen, F. Wu, Y.Q. Cheng, Z.R. Zhang, *J. Alloys Compd.* **823**, 153886 (2020)
11. Z.Z. Niu, Y.Z. Wang, C. Geng, J.X. Yan, Y. Wang, *J. Alloys Compd.* **820**, 153273 (2020)
12. T.K. Tsao, A.C. Yeh, C.M. Kuo, K. Kakehi, H. Murakami, J.W. Yeh, S.R. Jian, *Sci. Rep.* **7**, 12658 (2017)
13. X. Yan, Y. Zhang, *Scr. Mater.* **187**, 188 (2020)
14. J.W. Yeh, S.J. Lin, *J. Mater. Res.* **33**, 3129 (2018)
15. F. Otto, A. Doluh, C.H. Somsen, H. Bei, G. Eggeler, E.P. George, *Acta Mater.* **61**, 5743 (2013)
16. D.X. Wei, X.Q. Li, S. Schoecker et al., *Acta Mater.* **181**, 318 (2019)
17. Z.G. Wang, W. Zhou, J.F. Wang, R.C. Luo, X.C. Han, B. Chen, X.D. Wang, *Mater. Sci. Eng. A Struct.* **696**, 503 (2017)
18. Y.P. Lu, Y. Dong, S. Guo, L. Jiang, H.J. Kang, T.M. Wang, B. Wen, Z.J. Wang, J.C. Jie, Z.Q. Cao, H.H. Ruan, T.J. Li, *Sci. Rep. UK* **4**, 6200 (2014)
19. Y. Dong, K.Y. Zhou, Y.P. Lu, X.X. Gao, T.M. Wang, T.J. Li, *Mater. Des.* **57**, 67 (2014)
20. Y.P. Lu, X.Z. Gao, L. Jiang, Z.M. Chen, T.M. Wang, J.C. Jie, H.J. Kang, Y.B. Zhang, S. Guo, H.H. Ruan, Y.H. Zhao, Z.Q. Cao, T.J. Li, *Acta Mater.* **124**, 143 (2017)
21. X. Huang, Y. Dong, S.M. Lu, C.Q. Li, Z.R. Zhang, *Acta Metall. Sin. Engl.* **34**, 1079 (2021)
22. M.L. Wang, Y.P. Lu, T.M. Wang, C. Zhang, Z.Q. Cao, T.J. Li, P.K. Liaw, *Scr. Mater.* **204**, 114132 (2021)
23. X. Jin, Y.X. Liang, L. Zhang, J. Bi, Y. Zhou, B.S. Li, *Mater. Sci. Eng. A Struct.* **745**, 137 (2019)
24. P.J. Shi, R.G. Li, Y. Li, Y.B. Wen, W.L. Ren, Z. Shen, T.X. Zheng, J.C. Peng, X. Liang, P.F. Hu, N. Min, Y. Zhang, Y. Ren, P.K. Liaw, D. Raabe, Y.D. Wang, *Science* **373**, 912 (2021)
25. Q.Q. Ding, Y. Zhang, X. Chen, X.Q. Fu, D.K. Chen, S.J. Chen, L. Gu, F. Wei, H.B. Bei, Y.F. Gao, H.R. Wen, J.X. Li, Z. Zhang, T. Zhu, R.O. Ritchie, Q. Yu, *Nature* **574**, 223 (2019)
26. Z.M. Li, K.G. Pradeep, Y. Deng, D. Raanbe, C.C. Tasan, *Nature* **534**, 227 (2016)
27. E. Eshed, S.A. Majid, M. Bamberger, S. Osovski, *Front. Mater.* **7**, 284 (2020)
28. Y. Dong, X.X. Cao, Y.P. Lu, T.J. Li, *Mater. Lett.* **169**, 62 (2016)
29. U. Hecht, S. Gein, O. Stryzhyboroda, E. Eshed, S. Osovski, *Front. Mater.* **7**, 287 (2020)
30. W.N. Jiao, T.X. Li, X.X. Chang, Y.P. Lu, G.M. Yin, Z.Q. Cao, T.J. Li, *J. Alloys Compd.* **902**, 163814 (2022)
31. X. Jin, J. Bi, L. Zhang, Y. Zhou, X.Y. Du, Y.X. Liang, B.S. Li, *J. Alloys Compd.* **770**, 655 (2019)

32. Y.N. Guo, H.J. Su, P.X. Yang, Y. Zhao, Z.L. Shen, Y. Liu, D. Zhao, H. Jiang, J. Zhang, L. Liu, H.Z. Fu, *Acta Metall. Sin. Engl.* **35**, 1407 (2022)
33. Y.N. Guo, H.J. Su, H.T. Zhou, Z.L. Shen, Y. Liu, J. Zhang, L. Liu, H.Z. Fu, *J. Mater. Sci. Technol.* **111**, 298 (2022)
34. X.Y. Li, X.J. Gao, H.G. Lu, C.C. Shi, N.N. Guo, F.S. Yin, G.M. Zhu, *J. Mater. Res. Technol.* **17**, 865 (2022)
35. Y. Dong, Y.P. Lu, J.R. Kong, J.J. Zhang, T.J. Li, *J. Alloys Compd.* **573**, 96 (2013)
36. H. Jiang, H.Z. Zhang, T.D. Huang, Y.P. Lu, T.M. Wang, T.J. Li, *Mater. Des.* **109**, 539 (2016)
37. Z.Z. Niu, J. Xu, T. Wang, N.R. Wang, Z.H. Han, Y. Wang, *Intermetallics* **112**, 106550 (2019)
38. L. Pan, A.J. Liu, L. Wang, X.W. Cheng, *Mater. Lett.* **308**, 131250 (2022)
39. Y. Zhang, Y.J. Zhou, P.J. Lin, G.L. Chen, P.K. Liaw, *Adv. Eng. Mater.* **10**, 534 (2008)
40. S. Guo, C. Ng, J. Lu, C.T. Liu, *J. Appl. Phys.* **109**, 103505 (2011)
41. Y. Dong, Y.P. Lu, L. Jiang, T.M. Wang, T.J. Li, *Intermetallics* **52**, 105 (2014)
42. Y. Dong, Y.P. Lu, *Arab. J. Sci. Eng.* **44**, 803 (2019)
43. Y. Dong, *Fundamental study on microstructure and mechanical properties in multi-phase Al-Cr-Fe-Ni-M high entropy alloys*, PhD Dissertation, Dalian University of Technology (2016)

**Publisher's Note** Springer Nature remains neutral with regard to jurisdictional claims in published maps and institutional affiliations.

Springer Nature or its licensor (e.g. a society or other partner) holds exclusive rights to this article under a publishing agreement with the author(s) or other rightsholder(s); author self-archiving of the accepted manuscript version of this article is solely governed by the terms of such publishing agreement and applicable law.